














Elastic scattering of ${}^8\text{B} + {}^{\text{nat}}\text{Zr}$ at the sub-barrier energy of 26.5 MeV

K. Palli ^{1,2} A. Pakou ^{1,*} P. D. O'Malley,³ L. Acosta ^{4,5} A. M. Sánchez-Benítez,⁶ G. Souliotis ² A. M. Moro ^{7,8}
 E. F. Aguilera,⁹ E. Andrade,⁴ D. Godos ⁴ O. Sgouros ^{10,11} V. Soukeras ^{10,11} C. Agodi ¹⁰ T. L. Bailey ³
 D. W. Bardayan,³ C. Boomershine ³ M. Brodeur,³ F. Cappuzzello ^{10,11} S. Carmichael,³ M. Cavallaro,¹⁰ S. Dede,^{3,12}
 J. A. Dueñas,¹³ J. Henning,³ K. Lee,³ W. S. Porter,³ F. Rivero,³ and W. von Seeger ³

¹*Department of Physics and HINP, The University of Ioannina, 45110 Ioannina, Greece*

²*Department of Chemistry, National and Kapodistrian University of Athens and HINP, 15771 Athens, Greece*

³*Department of Physics and Astronomy, University of Notre Dame, Notre Dame, Indiana 46556, USA*

⁴*Instituto de Física, Universidad Nacional Autónoma de México, A.P. 20-364, Mexico City 01000, Mexico*

⁵*Instituto di Estructura de la Materia, CSIC, 28006 Madrid, Spain*

⁶*Departamento de Ciencias Integradas y Centro de Estudios Avanzados en Física, Matemáticas y Computación, Universidad de Huelva, 21071 Huelva, Spain*

⁷*Departamento de Física Atómica, Molecular y Nuclear, Universidad de Sevilla, Apartado 1065, E-41080 Sevilla, Spain*

⁸*Instituto Interuniversitario Carlos I de Física Teórica y Computacional (iCI), Apartado 1065, E-41080 Sevilla, Spain*

⁹*Departamento de Aceleradores y Estudio de Materiales, Instituto Nacional de Investigaciones Nucleares, Apartado Postal 18-1027, Código Postal 11801, Mexico, Distrito Federal, Mexico*

¹⁰*INFN Laboratori Nazionali del Sud, via S. Sofia 62, 95125 Catania, Italy*

¹¹*Dipartimento di Fisica e Astronomia "Ettore Majorana", Università di Catania, via S. Sofia 64, 95125 Catania, Italy*

¹²*Cyclotron Institute, Texas A&M University, College Station, Texas 77843, USA*

¹³*Centro de Estudios Avanzados en Física, Matemáticas y Computación, Universidad de Huelva, 21071 Huelva, Spain*



(Received 5 April 2024; accepted 17 May 2024; published 14 June 2024)

The reaction dynamics for the proton halo nucleus ${}^8\text{B} + {}^{\text{nat}}\text{Zr}$ is explored through an elastic scattering measurement at the sub-Coulomb barrier energy of 26.5 MeV. The differential angular distribution has been measured and the total reaction cross section as well as the interaction distance are derived via an optical model analysis. The present result is combined with relevant values for ${}^8\text{B}$ in comparison with ${}^6\text{He}$, ${}^7\text{Be}$, ${}^{6,7}\text{Li}$, and ${}^{16}\text{O}$ on various targets through a consistent optical model analysis at sub- and near-barrier energies. The results demonstrate the proton halo nature of this exotic nucleus, which exhibits larger values for both the total reaction and interaction radii observables, than those determined for the proton-rich radioactive nucleus ${}^7\text{Be}$ as well as for other stable weakly bound projectiles. Similar results are found for the neutron halo nucleus ${}^6\text{He}$. The present elastic scattering results are also described well with continuum-discretized coupled-channels calculations, exhibiting a weak coupling to continuum.

DOI: [10.1103/PhysRevC.109.064614](https://doi.org/10.1103/PhysRevC.109.064614)

I. INTRODUCTION

Research studies with weakly bound nuclei, especially those with large neutron-proton asymmetry, have opened new avenues in nuclear physics in the last decades. Here, the nuclear force and nuclear structure with the final goal, the impact on heavy-ion synthesis, have to be reconsidered. Clustering structures or the diffused surface of one or two neutrons or protons residing in the classical forbidden region outside a core, the well-known case of halo nuclei, have changed our thinking and offer unexpected phenomena for investigation [1–5]. The radii of such nuclei as well as the interaction distances and the strong absorption radii do not obey standard relations and values [6,7]. Distances and radii play an important role in the definition of the static properties of nuclei and in the determination of phenomenological potentials.

${}^8\text{B}$ is one of the most challenging proton-halo light nuclei with a breakup threshold of only 136 keV. It is produced in very few radioactive beam facilities around the world and, in view of its interesting structure and its dynamical behavior in nuclear reactions, any piece of information about it should be very important. Elastic scattering of weakly bound and/or exotic nuclei has proven to be a fundamental tool for revealing important features for them [8–10]. Channel coupling mechanisms, particularly at near-barrier energies, are very strong, since the competition between compound and direct mechanisms changes abruptly at the barrier and below it [11,12]. Furthermore, through elastic scattering, the determination of the total reaction cross section helps to identify the influence of specific nuclear structure properties of the collision partners, and in particular, at below-barrier energies a wealth of information may be unrevealed for unknown reaction mechanisms [13–15].

To investigate coupling mechanisms when breakup channels are involved, a standard method is the

*Contact author: apakou@uoi.gr

continuum-discretized coupled-channels (CDCC) approach, which has been extensively applied to two- and three-body projectiles [16–19], to study near-barrier elastic scattering and its associated direct reactions. These investigations have shown that strong couplings to direct channels are not always directly connected to the observation of large breakup or transfer cross sections [20]. In the context of coupling effects for radioactive nuclei with large proton-neutron asymmetry, other interesting results are the rainbow suppression, clearly observed in ${}^6\text{He}$ [21,22] and ${}^{11}\text{Be}$ [23,24] due to Coulomb dipole couplings or/and nuclear couplings. Such a suppression is also seen for the weakly bound but stable nucleus ${}^6\text{Li}$ on lead but not for ${}^7\text{Li}$ [25]. Another interesting case is that for the radioactive nucleus ${}^{11}\text{Li}$, which exhibits a dramatic deviation from Rutherford scattering at Coulomb barrier energies [26]. On the contrary, for ${}^8\text{B}$ no such dramatic phenomena have been reported at sub- and near-barrier energies. Instead, for systems like ${}^8\text{B} + {}^{208}\text{Pb}$ and ${}^8\text{B} + {}^{120}\text{Sn}$ weak couplings at energies close and below the barrier [10,12,27] have been reported, despite the very large breakup cross sections which exhaust all reaction probability at very deep sub-barrier energies [12].

Following the above motivation, we will present in this article the results of a measurement for the elastic scattering of ${}^8\text{B} + \text{natZr}$ at an incident energy of 26.5 MeV, which is 0.88 the nominal Coulomb barrier value. A phenomenological analysis will be used for the determination of the total reaction cross section as well as for the derivation of the critical interaction distance. The total reaction cross section will be considered in two reduction procedures in order to be compared with previous results with other targets as well as with other weakly bound and well-bound projectiles. The measured elastic scattering cross sections will be compared also with CDCC calculations.

In Sec. II, the experimental technique will be presented. In Secs. III and IV, the phenomenological and CDCC analyses will be presented and discussed. Finally, in Sec. V we will summarize the main results and conclusions of this work.

II. EXPERIMENTAL DETAILS AND RESULTS

The experiment was performed at the radioactive beam facility of the University of Notre Dame at the newly upgraded facility Trisol [28]. Details of the experiment are given in Ref. [29], where the elastic scattering experiment for ${}^7\text{Be} + \text{natZr}$ is presented with data collected under the same experimental conditions. The secondary ${}^8\text{B}$ beam was produced in-flight as part of a cocktail beam together with ${}^7\text{Be}$ and ${}^7\text{Li}$. The production was accomplished by using the reaction ${}^3\text{He} + {}^6\text{Li}$ with the two proton transfer channel ${}^3\text{He}({}^6\text{Li}, n){}^8\text{B}$ leading to ${}^8\text{B}$. A primary bunched beam of ${}^6\text{Li}$ was accelerated at 37 MeV by the UND FN tandem and impinged on a 2.5-cm-long gas target of ${}^3\text{He}$ at a pressure of 850 Torr. Secondary beams were produced at energies of 27.7 MeV for ${}^8\text{B}$, 20.1 MeV for ${}^7\text{Be}$, and 14.9 MeV for ${}^7\text{Li}$. The reaction products were then focused and guided by the three superconducting solenoids to a natZr target of 1.95 mg/cm² thickness. In the middle of the target, the beam energies

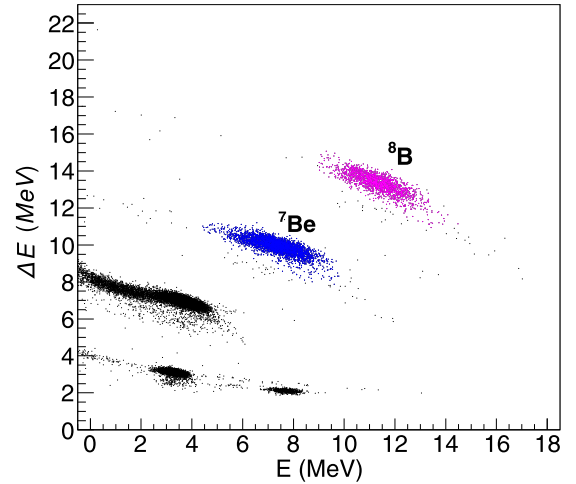


FIG. 1. Two dimension ΔE - E spectra, collected by a middle strip of one of our forward telescopes. The subtending angle is $\theta_{\text{lab}} = 25^\circ$.

correspond to 26.5 MeV, 19.2 MeV, and 14.3 MeV for ${}^8\text{B}$, ${}^7\text{Be}$, and ${}^7\text{Li}$, respectively. The reaction products, including elastically scattered particles, were detected in four two-stage ΔE - E telescopes. Each of these consisted of a double-sided silicon strip detector (DSSSD) and a pad silicon detector. Three of the telescopes were provided by the SIMAS (Sistema Móvil de Alta Segmentación) array of LEMA (Laboratorio Nacional de Espectrometría de Masas con Aceleradores) of the Physics Institute of the Autonomous National University of Mexico, and had DSSSDs with thickness of 20 μm , while the fourth one was provided by the Laboratorio de Interacciones Fundamentales (LIFE) of the research center of the Centro de Estudios Avanzados en Física, Matemáticas y Computación of the University of Huelva, Spain with its DSSSD 15 μm thick. The silicon pad detectors were either 130 or 500 μm thick. The dimensions for the telescopes were 5.4×5.4 cm. Each DSSSD consists of 16 vertical and 16 horizontal strips providing the possibility for interstrip rejection and pixel-by-pixel analysis. The telescopes covered an angular range between $\approx 20^\circ$ to 60° in the forward direction, and $\approx 110^\circ$ to 150° in the backward direction, positioned at 59.9 mm far from the target. In this respect each strip allocated an angular range of 3° , and therefore for each angle an uncertainty of 1.5° can be considered in the definition of angles in this work. The elastically scattered ${}^8\text{B}$ nuclei were very well separated from the other beam products with the ΔE - E technique, as can be seen in Fig. 1. Therefore the rather bad energy resolution of ≈ 1.5 MeV and 2.5 MeV for the DSSSD and E detectors, respectively, mainly due to the target thickness (projectile energy loss of 2.4 MeV), did not affect our measurement. Further on inelastic excitation to the first resonance state of ${}^8\text{B}$ at 769.5 keV were not recorded by our detectors, since due to its short lifetime (width of resonance 35.6 keV- $\tau \approx 1 \times 10^{-20}$ sec) to be compared with a boron flight time from target to detectors of ≈ 2.4 ns) were fully decayed before to reach our detectors. Ratios of differential cross sections over Rutherford scattering were formed taking into account our elastic scattering

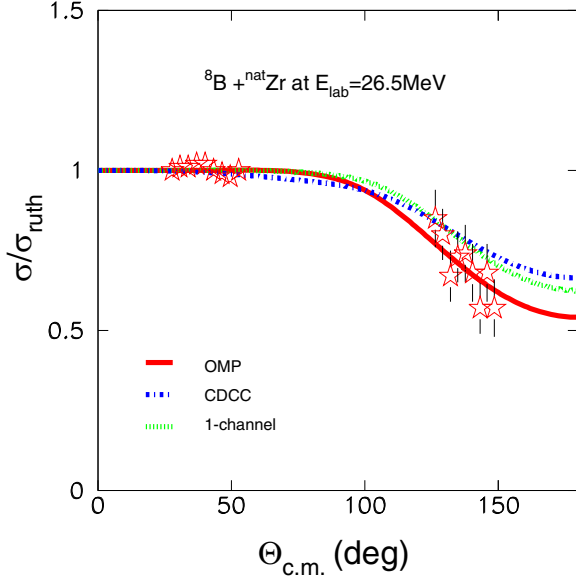


FIG. 2. Elastic scattering differential cross section for ${}^8\text{B} + {}^{\text{nat}}\text{Zr}$ at 26.5 MeV (projectile energy in the middle of the target) relative to the Rutherford cross section. Experimental data from the present work (open star symbols) are compared with OMP calculations consisting of a double-folding potential with the BDM3Y1 effective interaction (solid red line) as well as with CDCC calculations (dotted-dashed blue line). The green dotted line is the CDCC calculation omitting the coupling to the breakup channels. The depicted uncertainty in the cross sections is solely due to statistics, while an angular uncertainty of 1.5° should be considered for the angles.

measurements with ${}^7\text{Be} + {}^{\text{nat}}\text{Zr}$ under the same experimental conditions using the following relation:

$$\frac{\sigma_{s_B}(\theta)}{\sigma_{\text{Ruth}}^{s_B}(\theta)} = \frac{N_{s_B}(\theta)\sigma_{7\text{Be}}(\theta)}{N_{7\text{Be}}(\theta)\sigma_{\text{Ruth}}^{7\text{Be}}(\theta)} f, \quad (1)$$

where $N_{s_B}(\theta)$ and $N_{7\text{Be}}(\theta)$ are the elastic scattering yields of ${}^8\text{B}$ and ${}^7\text{Be}$ at an angle θ and $\sigma_{\text{Ruth}}^{s_B}(\theta)$, $\sigma_{\text{Ruth}}^{7\text{Be}}(\theta)$ the Rutherford cross sections for ${}^8\text{B}$ and ${}^7\text{Be}$ at an angle θ , respectively. f is a normalization factor determined at forward angles where the ratio should be equal to 1, due to Rutherford elastic scattering. In this respect, the differential angular distribution is free of uncertainties due to flux, target thickness and solid angle. The results are presented in Fig. 2.

III. PHENOMENOLOGICAL ANALYSIS

A. Optical model analysis

An optical model analysis was performed to deduce both the total reaction cross section and the critical interaction radius, d_I , to be described in the following section. These optical model calculations were performed with the ECIS code [30] with the real part of the entrance potential determined within the double-folding model [31] with the BDM3Y1 interaction developed by Khoa *et al.* [32]. The required matter densities for the double-folded potential were obtained from electron scattering data for ${}^{90}\text{Zr}$, adopting a three-parameter Gaussian model [33] and from the nuclear charge density

of Refs. [34,35] for ${}^8\text{B}$, by unfolding the proton charge distribution and making the isoscalar assumption, i.e., $\rho_{\text{Nuc}} = 1 + (N/Z)\rho_p$. For the imaginary part of the OMP we adopt the same form as for the real part, assuming the same radial dependence for both but using a different normalization factor. Our calculations were best fitted to the elastic scattering data, obtaining normalization factors of $N_R = 0.97 \pm 0.40$, $N_I = 0.86 \pm 0.40$ and a total reaction cross section of $\sigma = 180 \pm 40$ mb. In the following, it will be interesting to compare this value with the total reaction cross sections of its core ${}^7\text{Be}$ on the same or other targets, but also with other exotic and weakly bound nuclei and well-bound nuclei on various targets. Before that, in the following subsection we present another interesting nuclear property related to the reaction cross section, namely, the critical interaction distance.

B. Interaction distance

The interaction distance is a very important quantity, revealing gross features of elastic scattering within a semiclassical description where each scattering angle can be related to a classical trajectory. A critical interaction distance is one where the projectile begins to experience the nuclear force and due to absorption the ratio $\sigma/\sigma_{\text{Ruth}}$ drops below unity. We define here the *critical interaction distance* as the value D (see following equation) using the angle at which this ratio drops to 0.98 according to Guimarães *et al.* [7]. This is close to the value of 0.97 of our previous work [6]. The interaction distance, D , and the reduced interaction distance, d , are defined as follows, taking into account projectile energies close to the barrier where the ion moves primarily along a Coulomb trajectory

$$D = d(A_1^{1/3} + A_2^{1/3}) = \frac{1}{2}D_0 \left(1 + \frac{1}{\sin(\theta/2)} \right), \quad (2)$$

where

$$D_0 = \frac{Z_1 Z_2 e^2}{E_{\text{c.m.}}} \quad (3)$$

is the interaction distance of closest approach for a head-on collision, and A_1 , A_2 and Z_1 , Z_2 are the mass and atomic numbers for projectile and target, respectively. For our analysis, in addition to the present system ${}^8\text{B} + {}^{90}\text{Zr}$, we have considered also elastic scattering of the stable projectile ${}^{16}\text{O}$ on ${}^{58}\text{Ni}$, ${}^{90}\text{Zr}$, and ${}^{208}\text{Pb}$, the weakly bound but stable projectiles, ${}^6\text{Li}$ on ${}^{58}\text{Ni}$, ${}^{64}\text{Zn}$, ${}^{90}\text{Zr}$, ${}^{120}\text{Sn}$, ${}^{208}\text{Pb}$, and ${}^7\text{Li}$ on ${}^{58}\text{Ni}$, ${}^{64}\text{Zn}$, ${}^{120}\text{Sn}$, ${}^{118}\text{Sn}$, ${}^{208}\text{Pb}$, the radioactive neutron rich nucleus ${}^8\text{Li}$ on ${}^{208}\text{Pb}$, the radioactive proton rich nucleus ${}^7\text{Be}$ on ${}^{58}\text{Ni}$, ${}^{90}\text{Zr}$, ${}^{208}\text{Pb}$, the neutron halo nucleus ${}^6\text{He}$ on ${}^{58}\text{Ni}$, ${}^{64}\text{Zn}$, ${}^{120}\text{Sn}$, ${}^{208}\text{Pb}$, and the proton halo nucleus ${}^8\text{B}$ on ${}^{58}\text{Ni}$, ${}^{64}\text{Zn}$, ${}^{90}\text{Zr}$ (present data), ${}^{120}\text{Sn}$, ${}^{208}\text{Pb}$. Most of the above elastic scattering data were analyzed within the same optical model approach (see previous subsection) and the fitted angular distributions were transformed as a function of the reduced interaction distance. The critical interaction distances at $\sigma/\sigma_{\text{Ruth}} = 0.98$ were determined and are included in Table I. We should note that the results for ${}^8\text{Li}$ and ${}^6\text{He}$ on lead were taken from Ref. [7]. Furthermore, the calculations of the elastic scattering distributions for ${}^6\text{He}$ on ${}^{58}\text{Ni}$ and ${}^{120}\text{Sn}$ were

TABLE I. Critical reduced interaction distances, d_l , obtained by OMP analysis of present and previous elastic scattering data as given below (see also text). Relevant angles in the center of mass are also given. In both quantities an uncertainty at least of 10% should be assigned. Values marked with an asterisk were taken from the fits included in the associated reference. Values marked with a double asterisk were adopted from Ref. [7].

System	d_l (fm)	θ (deg)	Source
$^8\text{B}+^{58}\text{Ni}$	2.36	60	data from [40]
$^8\text{B}+^{64}\text{Zn}$	2.10*	72	data from [41]
$^8\text{B}+^{90}\text{Zr}$	2.25	64	present data
$^8\text{B}+^{120}\text{Sn}$	2.20	62	data from [27]
$^8\text{B}+^{208}\text{Pb}$	2.10	61	data from [42]
$^7\text{Be}+^{58}\text{Ni}$	2.04	78	data from [40]
$^7\text{Be}+^{90}\text{Zr}$	2.04	74	data from [29]
$^7\text{Be}+^{208}\text{Pb}$	1.85	78	data from [42]
$^{16}\text{O}+^{58}\text{Ni}$	1.8	94	data from [43]
$^{16}\text{O}+^{90}\text{Zr}$	1.69	102	data from [44]
$^{16}\text{O}+^{208}\text{Pb}$	1.67	92	data from [45]
$^6\text{Li}+^{58}\text{Ni}$	2.3	63	[46]
$^6\text{Li}+^{120}\text{Sn}$	2.1	67	[46]
$^6\text{Li}+^{208}\text{Pb}$	1.95	71	[25]
$^7\text{Li}+^{58}\text{Ni}$	2.3	63	[46]
$^7\text{Li}+^{120}\text{Sn}$	2.0	72	[46]
$^7\text{Li}+^{208}\text{Pb}$	1.8	81	[25]
$^6\text{He}+^{58}\text{Ni}$	2.37*	60	data from [36]
$^6\text{He}+^{120}\text{Sn}$	2.2*	62	data from [37]
$^6\text{He}+^{208}\text{Pb}$	2.2**		data from [47,48]
$^8\text{Li}+^{208}\text{Pb}$	2.3**		data from [49]

adopted from relevant references [36,37] and transformed versus interaction distance. Finally, all our results are included in Fig. 3, plotted as a function of the product of projectile and target atomic numbers, Z_1Z_2 . A very interesting result is revealed with this representation. Three different families are formed. One family, the top one in the figure, includes reduced critical interaction distances only for exotic projectiles: the neutron halo nucleus ^6He , the proton halo nucleus, ^8B , and the neutron skin ^8Li . All of these exhibit the same critical distance close to $d_l = 2.22$ fm. The best fitted line to these data, an almost parallel line to the x axis, is described by the equation

$$d_l = (-1.55078 \times 10^{-4} Z_1 Z_2 + 2.2542) \text{ fm} . \quad (4)$$

Details of the systems involved are depicted in Fig. 4. We should note here that unexpectedly the interaction distance for ^8Li is similar with those of the more exotic nuclei like ^6He and ^8B , although we know both from experiment and theory [38,39], that matter and charge radii for $^{6,7,8,9}\text{Li}$ nuclei are similar. The present result may indicate a neutron skin for ^8Li . However more results are necessary in this direction to draw firm conclusions for the structure of ^8Li .

Furthermore, another family, the bottom one in Fig. 3, includes the stable projectile ^{16}O together with ^7Li on ^{120}Sn and ^{208}Pb , which lie along the same curve and are well separated by a third family that includes weakly bound but stable nuclei

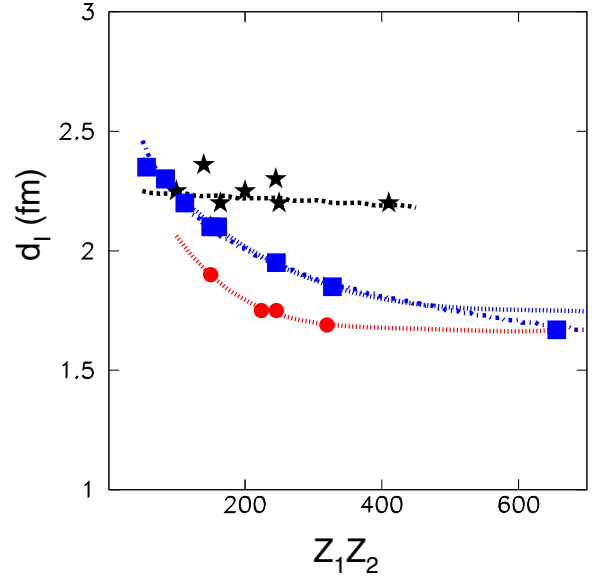


FIG. 3. Critical reduced interaction radii for various stable and radioactive projectiles on various targets plotted as a function of the product of the projectile and target atomic numbers. Three families are seen, which are further analyzed in Figs. 4–6.

such as ^6Li and the radioactive nucleus ^7Be , with binding energies lower than that of ^7Li . Details of the systems involved are shown in Figs. 5 and 6. Finally, another interesting point here is that an intersection point for the lines of stable and weakly bound projectiles occurs at the interaction distance of $^{16}\text{O}+^{208}\text{Pb}$. This may indicate that projectiles, either weakly bound or not, involved in elastic scattering where the product of the projectile and target atomic numbers is very large feel the nuclear interaction only when they get very close to each other. Although this is a plausible explanation, it has to be

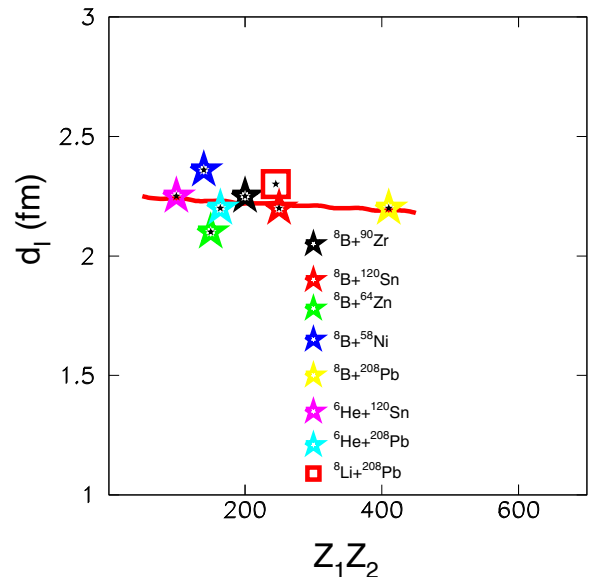


FIG. 4. Critical reduced interaction radii for exotic projectiles as indicated by the labels in the inset.

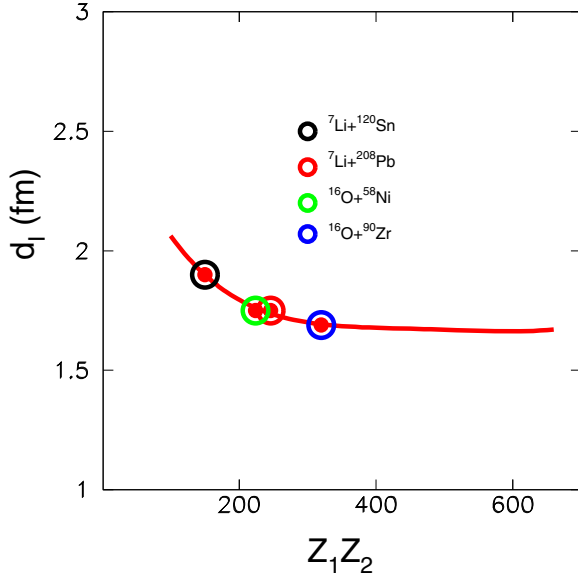


FIG. 5. Critical reduced interaction radii for ^{16}O and ^7Li projectiles as indicated by the labels in the inset.

tested experimentally with new data points for systems with atomic numbers product in the range $400 < Z_1 Z_2 < 600$. A supporting example comes from the weakly bound nucleus ^{17}F on lead, which presents a critical distance of $d_l = 1.69$ fm according to Ref. [7], close to that of the well bound nucleus ^{16}O . On the other hand, we cannot rule out a best-fit line to the weakly bound nuclei distances, not passing though the $^{16}\text{O} + ^{208}\text{Pb}$ but over passing it asymptotically (see Fig. 3 the dotted blue line).

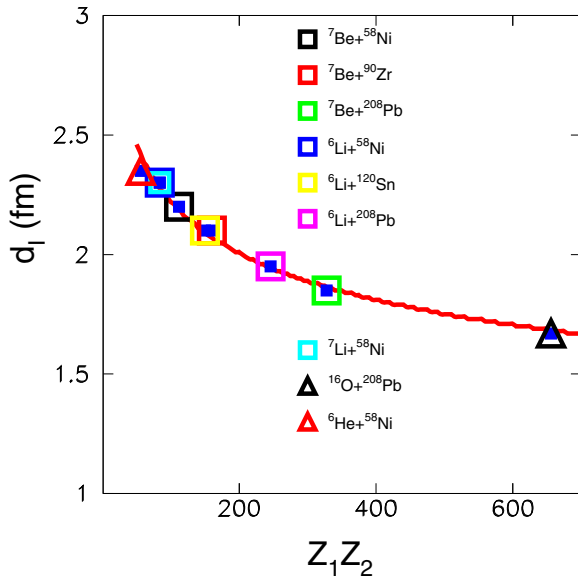


FIG. 6. Critical reduced interaction radii for various weakly bound projectiles as indicated by the labels in the inset. In the same curve, the radius for the reaction of the stable projectile ^{16}O on ^{208}Pb is also given.

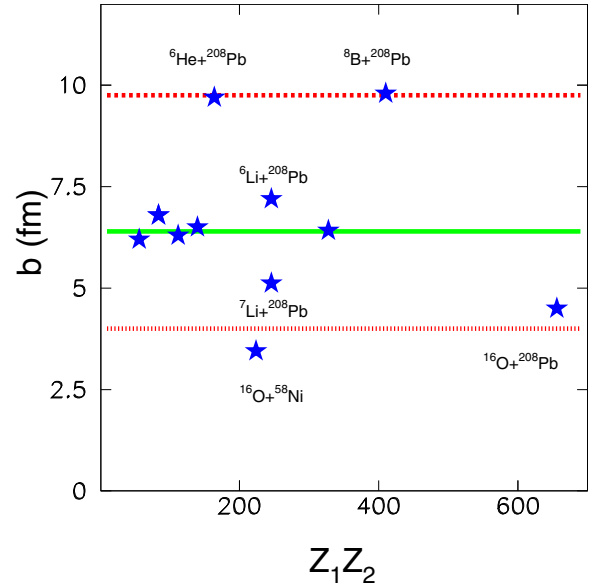


FIG. 7. Critical impact parameters for ^8B , ^6He , $^6,7\text{Li}$, ^{16}O on ^{58}Ni and ^{208}Pb targets at the critical distance D , corresponding to $\sigma(\theta)/\sigma_{\text{Ruth}}(\theta) = 0.98$. We note that values for $^8\text{B} + ^{58}\text{Ni}$, $^6\text{He} + ^{208}\text{Pb}$, $^6,7\text{Li} + ^{58}\text{Ni}$, $^7\text{Be} + ^{58}\text{Ni}$, and $^7\text{Be} + ^{208}\text{Pb}$, are located around the dotted green line at $b = 6.4$ fm. The only exception were the two data for ^6Li and ^7Li on ^{208}Pb located on either side but close to the $b = 6.4$ fm line with $b = 7.8$ fm and $b = 5.2$ fm, respectively.

The lines displayed in Figs. 3–6 are given by the following equations. For stable and well-bound nuclei with high breakup threshold, i.e., red line in Fig. 3:

$$d_l = 1.8469 \times 10^{-11} (Z_1 Z_2)^4 - 3.5384 \times 10^{-8} (Z_1 Z_2)^3 + 2.52699 \times 10^{-5} (Z_1 Z_2)^2 - 0.008056 (Z_1 Z_2) + 2.6489, \quad (5)$$

and for stable and radioactive weakly bound (dotted-dashed blue line in Fig. 3) by the equation

$$d_l = 4.3781 (Z_1 Z_2)^{-0.147357} \quad (6)$$

or (dotted blue line in Fig. 3) by the equation

$$d_l = -3.14275 \times 10^{-9} (Z_1 Z_2)^3 + 5.917165 \times 10^{-6} (Z_1 Z_2)^2 - 3.76299 \times 10^{-3} (Z_1 Z_2) + 2.55938. \quad (7)$$

In terms of the impact parameters and at the point where $\sigma/\sigma_{\text{Ruth}} = 0.98$, we plot in Fig. 7 critical impact parameter values obtained according to the following equation (see Ref. [50]):

$$b = \frac{l}{k} = \frac{D_0}{2} \cot \frac{\theta}{2} = \sqrt{(D(D - D_0))} \quad (8)$$

for the reactions of ^6He , ^8B , ^6Li , ^7Li , ^{16}O on ^{58}Ni and ^{208}Pb , that is, for the lightest and heaviest targets used in this analysis. It is remarkable that again here the representation of critical impact parameters as a function of the atomic number product for projectile and target reveals the following interesting point. For exotic light projectiles on heavy targets, the critical impact parameters are similar and very large, close to

10 fm. For stable projectiles on light and heavy targets they are close to 4 fm, with a weak mass dependence for ^{58}Ni and ^{208}Pb targets. Finally, for all other systems, either exotic (^6He , $^8\text{B} + ^{58}\text{Ni}$), radioactive weakly bound (^7Be on ^{58}Ni and ^{208}Pb) or weakly bound stable ($^{6,7}\text{Li} + ^{58}\text{Ni}$), they are located at a line of 6.4 fm. The only exceptions are the critical impact parameters for $^6\text{Li} + ^{208}\text{Pb}$ and $^7\text{Li} + ^{208}\text{Pb}$, located in either side of the 6.4 fm line with $b = 7.2$ fm and $b = 5.2$ fm, respectively.

From the previous observations, we extract the following conclusions, referred to energies close to the Coulomb barrier:

- (i) The plot of critical reduced interaction distances as a function of the product of atomic numbers for projectile-target, itemize the values in three categories possibly related with the breakup threshold.
- (ii) Critical reduced interaction distances values for light exotic nuclei (^6He , ^8B) with any target are almost the same and close to $d_I = 2.2$ fm.
- (iii) Critical reduced interaction distances for stable projectiles like ^{16}O and the weakly bound ^7Li belong to a second family with smaller values, described by a fourth degree polynomial, Eq. (5).
- (iv) Critical reduced interaction distances for all other weakly bound nuclei, radioactive or stable, belong to a third major family and can be represented by an exponential function, Eq. (6).
- (v) In terms of critical impact parameters, the highest values are found for exotic projectiles on heavy targets ($b \approx 10$ fm) and the lowest for well-bound projectiles ($b \approx 4$ fm). This indicates that for exotic projectiles on heavy targets, the absorption from elastic to direct processes starts at very large impact distances, while stable projectiles have to approach very close to the target in order to feel the nuclear attraction. For weakly bound and exotic nuclei on lower-mass targets, the attraction is felt at rather large values, $b \approx 6.4$ fm, but lower than that for exotic nuclei on heavy targets.
- (vi) Apart from differences between weakly bound and well-bound nuclei, differences between scattering on light or heavy targets should be underlined here, with emphasis not only on the structure of nuclei but also on the geometrical nature of scattering.

C. Comparison of total reaction cross sections

In this study, we have obtained the total reaction cross section of $^8\text{B} + ^{90}\text{Zr}$ as $\sigma = 180 \pm 40$ mb, analyzing new elastic scattering data at 26.5 MeV. In the same context, described in Sec. II. B, we have reanalyzed previous elastic scattering data for ^8B on various targets and data for various weakly bound projectiles, ^7Be , $^{6,7}\text{Li}$ on various targets. Data for ^6He were not reanalyzed but we have adopted results from relevant references (see Table I). From this analysis, we have obtained interaction distances, presented in the previous subsection and total reaction cross sections to be presented here. Systems considered in this analysis are $^8\text{B} + ^{90}\text{Zr}$ (present data), $^8\text{B} + ^{58}\text{Ni}$, $^8\text{B} + ^{120}\text{Sn}$, $^8\text{B} + ^{208}\text{Pb}$,

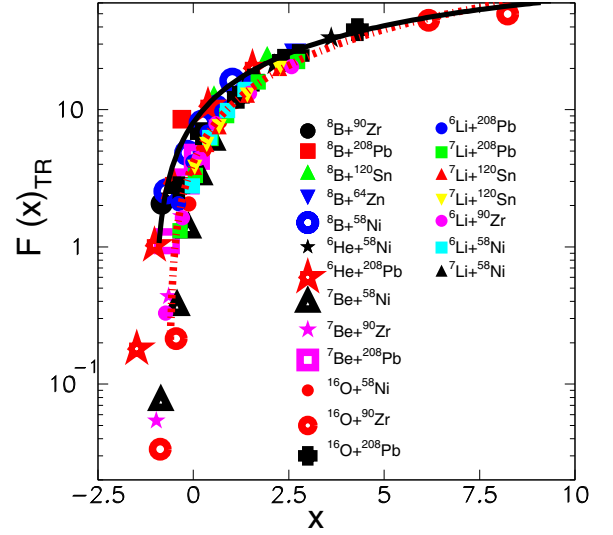


FIG. 8. Reduced total reaction cross sections for ^8B , ^6He , ^7Be , $^{6,7}\text{Li}$, ^{16}O on various targets, as indicated by the labels in the inset. The lines are best fits to data for ^8B , ^6He , shown with the solid black line, and for ^7Be , $^{6,7}\text{Li}$, and ^{16}O , shown with the dotted-dashed red line.

$^8\text{B} + ^{64}\text{Zn}$, $^7\text{Be} + ^{58}\text{Ni}$, $^7\text{Be} + ^{90}\text{Zr}$, $^7\text{Be} + ^{208}\text{Pb}$, $^6\text{He} + ^{58}\text{Ni}$, $^6\text{He} + ^{64}\text{Zn}$, $^6\text{He} + ^{120}\text{Sn}$, $^6\text{He} + ^{208}\text{Pb}$, $^6\text{Li} + ^{58}\text{Ni}$, $^6\text{Li} + ^{64}\text{Zn}$, $^6\text{Li} + ^{90}\text{Zr}$, $^6\text{Li} + ^{120}\text{Sn}$, $^6\text{Li} + ^{208}\text{Pb}$, $^7\text{Li} + ^{58}\text{Ni}$, $^7\text{Li} + ^{64}\text{Zn}$, $^7\text{Li} + ^{118,120}\text{Sn}$, $^7\text{Li} + ^{208}\text{Pb}$, $^{16}\text{O} + ^{58}\text{Ni}$, $^{16}\text{O} + ^{90}\text{Zr}$, and $^{16}\text{O} + ^{208}\text{Pb}$.

The main interest here is a reliable comparison between all the cross sections obtained. However, it is well known that the two more popular methods, Method I [51,52] and Method II [53] have been criticized for comparisons between very different systems [53]. However, we make an attempt to use both methods here, Method II modified, in order to extract some useful conclusions under some valid justifications.

In Method I, we adopt the same reduction procedure as for fusion cross sections following the authors of Ref. [51] who, motivated by the Wong approximation [54]

$$\sigma_F^W = R_B^2 \frac{\hbar\omega}{2E_{c.m.}} \ln \left[1 + \exp \left(\frac{2\pi(E_{c.m.} - V_B)}{\hbar\omega} \right) \right], \quad (9)$$

suggest that the fusion cross sections, σ_F , and the bombarding energy, $E_{c.m.}$, can be reduced by using the formulas

$$\sigma_F \rightarrow F(x) = \frac{2E_{c.m.}}{\hbar\omega R_B^2} \sigma_F, \quad (10)$$

corresponding to a c.m. energy $E_{c.m.}$ reduced to the quantity x given by the equation

$$E_{c.m.} \rightarrow x = \frac{E_{c.m.} - V_B}{\hbar\omega}. \quad (11)$$

According to the above relations and replacing σ_F with σ_R as in [52] (fusion with reaction cross section) total reaction cross section functions as a function of x , $F_{TR}(x)$, were formed and plotted in Fig. 8. The potential parameters, curvatures ($\hbar\omega$), radii (R_B), and potential heights (V_B), were deduced using the

TABLE II. Relevant potential properties: barrier V_B , radius R_B , and curvature $\hbar\omega$, used for the reduction of the reaction cross sections using Method I (see text).

System	V_B (MeV)	R_B (fm)	$\hbar\omega$ (MeV)
${}^8\text{B}+{}^{90}\text{Zr}$	28.28	9.475	4.736
${}^8\text{B}+{}^{58}\text{Ni}$	21.26	8.773	4.377
${}^8\text{B}+{}^{64}\text{Zn}$	22.4	8.934	4.42801
${}^8\text{B}+{}^{120}\text{Sn}$	33.59	10.007	4.963
${}^8\text{B}+{}^{208}\text{Pb}$	49.9	11.106	5.998
${}^6\text{He}+{}^{58}\text{Ni}$	8.27	9.056	3.150
${}^6\text{He}+{}^{64}\text{Zn}$	8.74	9.193	3.199
${}^6\text{He}+{}^{120}\text{Sn}$	13.24	10.18	3.653
${}^6\text{He}+{}^{208}\text{Pb}$	19.78	11.247	4.176
${}^7\text{Be}+{}^{58}\text{Ni}$	17.05	8.756	4.193
${}^7\text{Be}+{}^{90}\text{Zr}$	22.69	9.447	4.553
${}^7\text{Be}+{}^{208}\text{Pb}$	40.11	11.066	5.413
${}^6\text{Li}+{}^{90}\text{Zr}$	17.05	9.435	4.283
${}^6\text{Li}+{}^{58}\text{Ni}$	12.79	8.758	3.929
${}^6\text{Li}+{}^{64}\text{Zn}$	14.49	8.91	3.979
${}^6\text{Li}+{}^{120}\text{Sn}$	20.29	9.948	4.507
${}^6\text{Li}+{}^{208}\text{Pb}$	30.18	11.035	5.125
${}^7\text{Li}+{}^{58}\text{Ni}$	12.515	8.968	3.597
${}^7\text{Li}+{}^{120}\text{Sn}$	19.95	10.131	4.129
${}^7\text{Li}+{}^{118}\text{Sn}$	20.020	10.092	4.146
${}^7\text{Li}+{}^{208}\text{Pb}$	29.74	11.209	4.699
${}^8\text{Li}+{}^{208}\text{Pb}$	29.36	11.365	4.357
${}^{16}\text{O}+{}^{58}\text{Ni}$	31.82	9.425	3.851
${}^{16}\text{O}+{}^{90}\text{Zr}$	42.61	10.099	4.105
${}^{16}\text{O}+{}^{208}\text{Pb}$	76.08	11.689	4.755

Christensen-Winther potential [55] and the values obtained are included in Table II.

The aim of this reduction is to remove static effects associated with the details of the optical potential and therefore probe dynamic channel coupling effects. From an inspection of Fig. 8, we observe the expected spread of the data due to target dependence. However, this spread does not exceed 20% of the assigned values and, taking into account that the uncertainties of the calculated reaction cross sections are at least of the order of 10%, it seems justified to suggest the following: Two families of reduced total reaction cross sections are formed. In the upper part, cross sections for the exotic nuclei ${}^8\text{B}$ and ${}^6\text{He}$, which were fitted with a second-order polynomial, shown with the black solid line. At the bottom, another family is seen that comprises data for the stable nucleus ${}^{16}\text{O}$, the weakly bound radioactive nucleus ${}^7\text{Be}$ and the weakly bound but stable ${}^{6,7}\text{Li}$ nuclei. These were fitted in the same way and the outcome of the fit is displayed with a dotted-dashed red line. As expected, the reduced reaction cross sections for exotic nuclei are larger (a factor of 2 around the barrier), from cross sections of stable or weakly bound projectiles. At energies well above the barrier no substantial difference occurs. At lower energies, however, below the barrier the difference becomes progressively larger. For example, the reduced cross section for ${}^8\text{B}+{}^{90}\text{Zr}$ at the sub-Coulomb barrier energy of 26.5 MeV, is higher by a factor of 12 from the relevant cross section of its core ${}^7\text{Be}+{}^{90}\text{Zr}$ (see Fig. 9). This

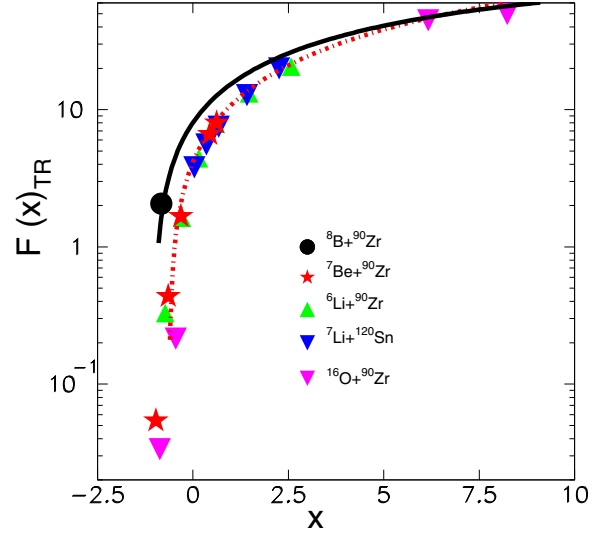


FIG. 9. Same as in Fig. 8 but only for weakly bound projectiles on the ${}^{90}\text{Zr}$ target. Due to the lack of data for ${}^7\text{Li}+{}^{90}\text{Zr}$, we include here data for ${}^7\text{Li}+{}^{120}\text{Sn}$.

fact indicates that under the barrier unexpected phenomena can occur, related to overwhelming direct processes [13–15], and the total reaction cross section is a good criterion for probing those. Furthermore, another interesting conclusion is that the neutron halo ${}^6\text{He}$, in gross features, behaves in the same way as the proton halo ${}^8\text{B}$, with respect to the total reaction cross section as well as to interaction distances as we saw in the previous section. This similarity between ${}^8\text{B}$ and ${}^6\text{He}$ was also noted before through total reaction cross sections in ${}^{58}\text{Ni}$ [40] and studying a possible decoupling between the neutron or the proton halo and the core of the exotic projectile [56].

Now we concentrate on Method II [53] modified by a multiplicative factor equal to the reduced critical interaction distance, d_I , as follows.

For the cross section

$$\sigma_R \rightarrow \frac{\sigma}{(d_I(A_1^{1/3} + A_2^{1/3}))^2}, \quad (12)$$

and for the energy

$$E_R \rightarrow \frac{E d_I (A_1^{1/3} + A_2^{1/3})}{Z_1 Z_2} \quad (13)$$

with (Z_1, A_1) and (Z_2, A_2) the atomic and mass numbers for projectile and target, respectively. Note the multiplicative factor d_I (reduced critical distance) in front of the sum $(A_1^{1/3} + A_2^{1/3})$, which constitutes our modification of Method II. Within this framework, we expect all physics related to breakup or other direct effects to be washed out for weakly bound nuclei, but not for the well-bound ones. Total reaction cross sections, reduced by the above equations, are plotted in Fig. 10, omitting results of ${}^{6,7}\text{Li}+{}^{208}\text{Pb}$, for the sake of clarity. Data for the ${}^{208}\text{Pb}$ target are presented separately in Fig. 11. The general conclusion from these plots is that under the presently suggested reduction with the modified Method II, all weakly bound projectiles, with the exception of ${}^{6,7}\text{Li}$ on ${}^{208}\text{Pb}$,

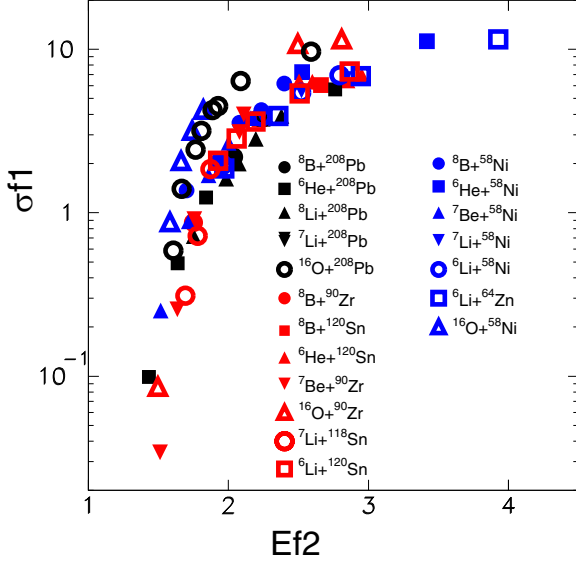


FIG. 10. Reduced total reaction cross sections for all systems studied in this work (excluding ${}^6\text{Li}+{}^{208}\text{Pb}$) on various targets as shown in the inset of the figure. The reduction was done according to Eqs. (12) and (13). The scaling factors are: $f_1 = 1/(d_I(A_1^{1/3} + A_2^{1/3}))^2$ and $f_2 = d_I(A_1^{1/3} + A_2^{1/3})/(Z_1Z_2)$.

are grouped around a curve very well separated from that of stable nuclei like ${}^{16}\text{O}$. We underline the fact that at large Z_1Z_2 the two curves end at the same point. An exception is ${}^6\text{Li}+{}^{208}\text{Pb}$, located between these curves and of ${}^7\text{Li}+{}^{208}\text{Pb}$, located near the curve of stable nuclei. We underline here the exception presented in the critical impact parameters for ${}^6\text{Li}$ and ${}^7\text{Li}+{}^{208}\text{Pb}$ (see Fig. 7). Further theoretical work may be needed to unravel the physics behind this exception. From the point of view of the energy dependence of the optical potential, this may not be unexpected. As was shown before in

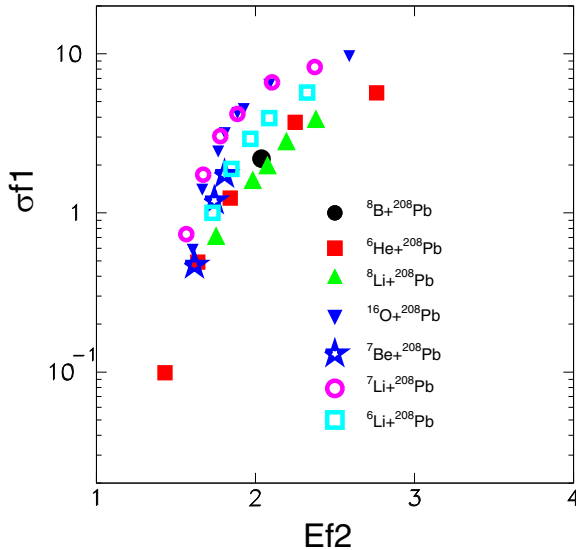


FIG. 11. Same as in Fig. 10, but only for a ${}^{208}\text{Pb}$ target and including the ${}^6,{}^7\text{Li}$ projectiles, as indicated by the labels in the inset.

a systematic work reported in Refs. [57,58], the energy dependence of the OM potential of ${}^7\text{Li}$ on heavy targets is clearly diverting from the one with light targets. For ${}^6\text{Li}$, although there is no systematic work on this topic, the indication is similar. For heavier targets the trend for the imaginary potential of ${}^6\text{Li}$ is very different from that for ${}^7\text{Li}$, where approaching the barrier from higher to lower energies an increasing trend is apparent and clearly seen, particularly for the heavier targets [8,59,60]. On the other hand, on the above systematic work for ${}^7\text{Li}$, it was further found that the behavior of ${}^7\text{Be}$ is similar to that of ${}^7\text{Li}$. This cannot be confirmed within this study, where the reduced cross sections for ${}^7\text{Be}$, when we take into account the interaction distance, follow the trend of ${}^6\text{Li}$ rather than that for ${}^7\text{Li}$. This cannot be further confirmed because the data are scarce and the estimated uncertainties large. Another interesting point emerged by adopting Method II, and replacing the critical distance, d_I with the one at the strong absorption radius corresponding to $\sigma/\sigma_{\text{Ruth}} \approx 0.25$. Our preliminary results in that direction indicate that most of the physics behind an effective reduced radius equal to the strong absorption radius, is washed out and all reduced cross sections are gathered to a band with an uncertainty of 50% irrespective of whether the systems involve well-bound or weakly bound exotic projectiles, in any target. In conclusion of the above, the dynamics of the reaction is different between well-bound and weakly-bound when the scattered nuclei begin to feel the nuclear interaction and $\sigma/\sigma_{\text{Ruth}} = 0.98$. At that time, direct reactions are the most prominent and for weakly bound nuclei overwhelm the total reaction cross section. On the other hand, when $\sigma/\sigma_{\text{Ruth}} = 0.25$ the colliding nuclei start a fusion process and the gross features of reactions with all projectiles are similar with variations due to their geometry and the persistence of direct reactions for weakly bound nuclei.

IV. CDCC CALCULATIONS

The measured elastic data have also been compared with CDCC calculations, assuming a three-body model for the reaction (${}^7\text{Be}+p+{}^{90}\text{Zr}$). The ${}^7\text{Be}+p$ interaction used to generate the ${}^8\text{B}$ ground and continuum states was taken from Ref. [61] and contains both central and spin-orbit terms. The ${}^7\text{Be}$ spin was ignored for simplicity. The ground state was assumed to consist of a pure $1p_{3/2}$ configuration. The proton- ${}^{90}\text{Zr}$ potential was taken from the global parametrization of Koning-Delaroche [62]. The ${}^7\text{Be}+{}^{90}\text{Zr}$ potential was taken from a double-folding calculation using a BDM3Y1 nucleon-nucleon interaction and normalization factors $N_r = 1.2$ $N_i = 0.476$ deduced from elastic scattering data of ${}^7\text{Be}+{}^{90}\text{Zr}$ at the appropriate energy, measured in the same experiment. Details can be found in [29]. The ${}^8\text{B}$ unbound states were represented by a set of ${}^7\text{Be}+p$ continuum bins up to a maximum energy $\varepsilon_{\text{max}} = 9$ MeV and a maximum orbital angular momentum $\ell_{\text{max}} = 6$. Coupling potentials included both nuclear and Coulomb couplings. The calculations were performed with the code FRESKO [63].

The calculated elastic differential cross section is compared with the data in Fig. 2. They agree with each other

within the experimental errors, although some overestimation of the experimental data is apparent.

To quantify the effect of the breakup channels on the elastic cross sections, we present also in this figure the CDCC calculations omitting these breakup couplings (green dotted line). The effect, although not negligible, is rather modest as compared to the case of neutron-halo nuclei. This result is consistent with previous findings for other reactions induced by ${}^8\text{B}$ [10,12,27].

The calculated total reaction cross section in these CDCC calculations is $\sigma = 370$ mb. This value is significantly larger than the value extracted from the OM fit of the measured elastic differential cross section ($\sigma = 180 \pm 40$ mb). We can see from Fig. 2 that the calculated ratio of differential cross sections versus Rutherford deviate from 1 at more forward angles than is predicted by the fit. Unfortunately this can not be validated experimentally due to lack of data at an angular range around $\theta_{c.m.} = 90^\circ$.

V. SUMMARY AND CONCLUSIONS

We have measured the angular distribution of elastic scattering for the proton-halo nucleus ${}^8\text{B}$ on a medium mass target, ${}^{\text{nat}}\text{Zr}$, at a sub-barrier energy of 26.5 MeV.

Using a phenomenological analysis, the total cross sections of the reaction and the critical interaction distances were deduced and compared with the results of reactions induced by its core, ${}^7\text{Be}$, the exotic ${}^6\text{He}$ and the weakly bound nuclei ${}^{6,7}\text{Li}$ on the same target, as well as, on other lighter (${}^{58}\text{Ni}$) and heavier (${}^{208}\text{Pb}$) targets. The main conclusions are:

- (i) The reduced total reaction cross section of ${}^8\text{B} + {}^{90}\text{Zr}$ at a sub-Coulomb barrier energy, eliminating static effects associated with the details of the optical potential, is ≈ 12 times higher than the relevant one of its core ${}^7\text{Be}$, indicating the halo nature of this exotic nucleus.
- (ii) Total reaction cross sections below barrier can be used effectively as probes for tracing variations between reaction mechanisms of weakly bound and well bound nuclei.
- (iii) Novel plots of reduced critical interaction distances versus the product of atomic numbers for projectile and target, $Z_1 Z_2$, probe gross features of the relevance of direct reaction mechanisms among exotic, weakly

bound and well bound projectiles. Moreover, they reveal similar features for ${}^8\text{B}$ and ${}^6\text{He}$ in contrast to other weakly bound projectiles and all of them at variance with well-bound nuclei.

- (iv) Similar plots in terms of the critical impact parameters confirm the above statement, revealing very large impact parameters for both ${}^8\text{B}$ and ${}^6\text{He} + {}^{208}\text{Pb}$ with $b \approx 10$ fm instead of $b \approx 4$ fm for well-bound projectiles and $b \approx 6.4$ fm for all other weakly bound on either target and for exotic on light-medium targets.
- (v) At sub- and near-barrier energies, the proton halo nucleus ${}^8\text{B}$ resembles the halo nucleus ${}^6\text{He}$, regarding the total reaction cross sections and critical interaction distances, where the projectile starts to feel the nuclear interaction and direct reaction channels are opened. However, the dynamics of reaction mechanisms may be different for each halo nucleus, due to their different structure, leading to a strong impact of non elastic channels on the ${}^6\text{He}$ elastic scattering and a weak impact in the case of ${}^8\text{B}$, the latter effect confirmed in this study.

Finally, our CDCC analysis corroborates previous findings for ${}^8\text{B}$ on heavy (${}^{208}\text{Pb}$) and medium-mass (${}^{120}\text{Sn}$) targets, demonstrating that the coupling to continuum is not substantial, despite the dynamics of direct reactions described above.

ACKNOWLEDGMENTS

We warmly acknowledge technical support from the personnel of the radioactive beam facility of the University of Notre Dame and M. Pérez-Vielma from the Autonomous National University of Mexico, for her technical support in the construction of the geometry used for the SIMAS+LIFE array. We acknowledge support from NSF Grants No. PHY-2011890 and No. PHY-2310059 of the University of Notre Dame. One of us (K.P.) acknowledges support from the Hellenic Foundation for Research and Innovation (HFRI) under the 4th Call for HFRI Ph.D. Fellowships, No. 009194, one (A.M.M.) by the Spanish Ministerio de Ciencias, Innovación y Universidades (including FEDER funds) under Project No. FIS2017-88410-P and by the European Union's Horizon 2020 research and innovation program under Grant Agreement No. 654002, and one (L.A.) by CONACYT 315839 and DGAPA-PAPIIT IG101423.

-
- [1] I. Tanihata, H. Savajols, and R. Kanungo, Recent experimental progress in nuclear halo structure studies, *Prog. Part. Nucl. Phys.* **68**, 215 (2013).
 - [2] I. Tanihata, H. Hamagaki, O. Hashimoto, Y. Shida, N. Yoshikawa, K. Sugimoto, O. Yamakawa, T. Kobayashi, and N. Takahashi, Measurements of interaction cross sections and radii of He isotopes, *Phys. Lett. B* **160**, 380 (1985).
 - [3] W. Nazarewicz, Challenges in nuclear structure theory, *J. Phys. G* **43**, 044002 (2016).
 - [4] C. Forssén, G. Hagen, M. Hjorth-Jensen, W. Nazarewicz, and J. Rotureau, Living on the edge of stability, the limits of the nuclear landscape, *Phys. Scr.* **2013**, 014022 (2013).
 - [5] R. Kanungo, Unveiling new features in rare isotopes with direct reactions, recent progress in few-body physics, in *Proceedings of the 22nd International Conference on Few-Body Problems in Physics*, Springer Proceedings in Physics, Vol. 238, edited by N. A. Orr, M. Płoszajczak, F. M. Marques, and J. Carbonell (Springer Nature Switzerland AG, Cham, Switzerland, 2018), p. 299.
 - [6] A. Pakou and K. Rusek, Interaction distances for weakly bound nuclei at near barrier energies, *Phys. Rev. C* **69**, 057602 (2004).
 - [7] V. Guimarães, J. Lubian, J. J. Kolata, E. F. Aguilera, M. Assunção, and V. Morcelle, Phenomenological critical

- interaction distance from elastic scattering measurements on a ^{208}Pb target, *Eur. Phys. J. A* **54**, 223 (2018).
- [8] L. F. Canto, P. R. S. Gomes, R. Donangelo, and M. S. Hussein, Fusion and breakup of weakly bound nuclei, *Phys. Rep.* **424**, 1 (2006).
- [9] L. F. Canto, V. Guimarães, J. Lubián, and M. S. Hussein, The total reaction cross section of heavy-ion reactions induced by stable and unstable exotic beams: The low-energy regime, *Eur. Phys. J. A* **56**, 281 (2020).
- [10] N. Keeley, N. Alamanos, K. W. Kemper, and K. Rusek, Elastic scattering and reactions of light exotic beams, *Prog. Part. Nucl. Phys.* **63**, 396 (2009).
- [11] A. Pakou, D. Pierroutsakou, M. Mazzocco, L. Acosta, and X. Aslanoglou, Total reaction cross sections for $^8\text{Li} + ^{90}\text{Zr}$ at near-barrier energies, *Eur. Phys. J. A* **51**, 55 (2015).
- [12] A. Pakou, L. Acosta, P. D. O'Malley, S. Aguilar, E. F. Aguilera, M. Baines, D. Bardayan, F. D. Becchetti, C. Boomershine, M. Brodeur, F. Cappuzzello, S. Carmichael, L. Caves, E. Chavez, C. Flores-Vazquez, A. Gula, J. J. Kolata, B. Liu, D. J. Marin-Lambarri, F. F. Morales, K. Rusek, A. M. Sanchez-Benitez, O. Sgouros, V. R. Sharma, V. Soukeras, and G. Souliotis, Dominance of direct reaction channels at deep sub-barrier energies for weakly bound nuclei on heavy targets: The case $^8\text{B} + ^{208}\text{Pb}$, *Phys. Rev. C* **102**, 031601(R) (2020).
- [13] A. Pakou, P. D. O'Malley, L. Acosta, A. M. Sánchez-Benitez, J. J. Kolata, K. Palli, O. Sgouros, V. Soukeras, and G. Souliotis, Searching for treasures at sub-barrier energies: The case of ^8B and ^7Be , *EPJ Web Conf.* **252**, 04006 (2021).
- [14] R. Raabe, J. L. Sida, J. L. Charvet, N. Alamanos, C. Angulo *et al.*, No enhancement of fusion probability by the neutron halo of ^6He , *Nature (London)* **431**, 823 (2004).
- [15] A. Lemasson, A. Shrivastava, A. Navin, M. Rejmund, N. Keeley *et al.*, Modern Rutherford experiment: Tunneling of the most neutron-rich nucleus, *Phys. Rev. Lett.* **103**, 232701 (2009).
- [16] N. Austern, Y. Iseri, M. Kamimura, M. Kawai, G. Rawitscher, and M. Yashiro, Continuum-discretized coupled-channels calculations for three-body models of deuteron-nucleus reactions, *Phys. Rep.* **154**, 125 (1987).
- [17] I. J. Thompson and F. M. Nunes, *Nuclear Reactions for Astrophysics: Principles, Calculation and Applications*, 1st ed. (Cambridge University Press, Cambridge, 2009).
- [18] M. Rodríguez-Gallardo, J. M. Arias, J. Gómez-Camacho, R. C. Johnson, A. M. Moro, I. J. Thompson, and J. A. Tostevin, Four-body continuum-discretized coupled-channels calculations using a transformed harmonic oscillator basis, *Phys. Rev. C* **77**, 064609 (2008).
- [19] M. Rodríguez-Gallardo, J. M. Arias, J. Gómez-Camacho, A. M. Moro, I. J. Thompson, and J. A. Tostevin, Four-body continuum-discretized coupled-channels calculations, *Phys. Rev. C* **80**, 051601(R) (2009).
- [20] N. Keeley, R. S. Mackintosh, and C. Beck, Breakup coupling effects on near-barrier ^6Li , ^7Be and $^8\text{B} + ^{58}\text{Ni}$ elastic scattering compared, *Nucl. Phys. A* **834**, 792c (2010).
- [21] O. R. Kakuee, M. A. G. Alvarez, M. V. Andrés, S. Cherubini, T. Davinson *et al.*, Long range absorption in the scattering of ^6He on ^{208}Pb and ^{197}Au at 27 MeV, *Nucl. Phys. A* **765**, 294 (2006).
- [22] L. Acosta, A. M. Sánchez-Benitez, M. E. Gómez, I. Martel, F. Pérez-Bernal *et al.*, Elastic scattering and α -particle production in $^6\text{He} + ^{208}\text{Pb}$ collisions at 22 MeV, *Phys. Rev. C* **84**, 044604 (2011).
- [23] A. Di Pietro, G. Randisi, V. Scuderi, L. Acosta, F. Amorini *et al.*, Elastic scattering and reaction mechanisms of the halo nucleus ^{11}Be around the Coulomb barrier, *Phys. Rev. Lett.* **105**, 022701 (2010).
- [24] N. Keeley, N. Alamanos, K. W. Kemper, and K. Rusek, Strong nuclear couplings as a source of Coulomb rainbow suppression, *Phys. Rev. C* **82**, 034606 (2010).
- [25] N. Keeley, S. J. Bennett, N. M. Clarke, B. R. Fulton, G. Tungate *et al.*, Optical model analyses of $^{6,7}\text{Li} + ^{208}\text{Pb}$ elastic scattering near the Coulomb barrier, *Nucl. Phys. A* **571**, 326 (1994).
- [26] M. Cubero, J. P. Fernandez-Garcia, M. Rodriguez-Gallardo, L. Acosta, M. Alcorta, M. A. G. Alvarez, M. J. G. Borge, L. Buchmann, C. A. Diget, H. A. Falou, B. R. Fulton, H. O. U. Fynbo, D. Galaviz, J. Gomez-Camacho, R. Kanungo, J. A. Lay, M. Madurga, I. Martel, A. M. Moro, I. Mukha, T. Nilsson, A. M. Sanchez-Benitez, A. Shotter, O. Tengblad, and P. Walden, Do halo nuclei follow Rutherford elastic scattering at energies below the barrier? The case of ^{11}Li , *Phys. Rev. Lett.* **109**, 262701 (2012).
- [27] L. Yang, C. J. Lin, H. Yamaguchi, A. M. Moro, N. R. Ma *et al.*, Breakup of the proton halo nucleus ^8B near barrier energies, *Nat. Commun.* **13**, 7193 (2022).
- [28] P. D. O'Malley, T. Ahn, D. W. Bardayan, M. Brödeur, S. Coil, and J. J. Kolata, TriSol: A major upgrade of the TwinSol RNB facility, *Nucl. Instrum. Methods Phys. Res. A* **1047**, 167784 (2023).
- [29] K. Palli, A. Pakou, A. M. Moro, P. D. O'Malley, L. Acosta, A. M. Sanchez-Benitez, G. Souliotis, E. F. Aguilera, E. Andrade, D. Godos, O. Sgouros, V. Soukeras, C. Agodi, T. L. Bailey, D. W. Bardayan, C. Boomershine, M. Brodeur, F. Cappuzzello, S. Carmichael, M. Cavallaro, S. Dede, J. A. Duenas, J. Henning, K. Lee, W. S. Porter, F. Rivero, and W. von Seeger, Quasielastic scattering of $^7\text{Be} + ^{\text{nat}}\text{Zr}$ at sub- and near-barrier energies, *Phys. Rev. C* **107**, 064613 (2023).
- [30] J. Raynal, Recurrence relations for distorted-wave Born approximation Coulomb excitation integrals and their use in coupled channel calculations, *Phys. Rev. C* **23**, 2571 (1981).
- [31] G. R. Satchler, Heavy-ion scattering and reactions near the Coulomb barrier and threshold anomalies, *Phys. Rep.* **199**, 147 (1991).
- [32] D. T. Khoa and W. von Oertzen, Refractive alpha-nucleus scattering: A probe for the incompressibility of cold nuclear matter, *Phys. Lett. B* **342**, 6 (1995).
- [33] C. W. De Jager, C. W. Jager, and C. De Vries, Nuclear charge-density-distribution parameters from elastic electron scattering, *At. Data Nucl. Data Tables* **14**, 479 (1974).
- [34] A. Bhagwat, Y. K. Gambhir, and S. H. Patil, Nuclear densities in the neutron-halo region, *Eur. Phys. J. A* **8**, 511 (2000).
- [35] N. Keeley (private communication).
- [36] V. Morcelle, K. C. C. Pires, M. Rodríguez-Gallardo, R. Lichtenthäler, and A. Lépine-Szily, Four-body effects in the $^6\text{He} + ^{58}\text{Ni}$ scattering, *Phys. Lett. B* **732**, 228 (2014).
- [37] P. N. de Faria, R. Lichtenthäler, K. C. C. Pires, A. M. Moro, A. Lépine-Szily, V. Guimarães, D. R. J. Mendes, Jr., A. Arazi, M. Rodríguez-Gallardo, A. Barioni, V. Morcelle, M. C. Morais, O. Camargo, Jr., J. Alcántara Nuñez, and M. Assuncao, Elastic scattering and total reaction cross section of $^6\text{He} + ^{120}\text{Sn}$, *Phys. Rev. C* **81**, 044605 (2010).
- [38] I. Tanihata, T. Kobayashi, O. Yamakawa, S. Shimoura, K. Ekuni *et al.*, Measurement of interaction cross sections using isotope

- beams of Be and B and isospin dependence of the nuclear radii, *Phys. Lett. B* **206**, 592 (1988).
- [39] W. Nörtershäuser, T. Neff, R. Sánchez, and I. Sick, Charge radii and ground state structure of lithium isotopes: Experiment and theory reexamined, *Phys. Rev. C* **84**, 024307 (2011).
- [40] E. F. Aguilera, E. Martínez-Quiroz, D. Lizcano, A. Gómez-Camacho, J. J. Kolata, L. O. Lamm, V. Guimarães, R. Lichtenthäler, O. Camargo, F. D. Becchetti, H. Jiang, P. A. DeYoung, P. J. Mears, and T. L. Belyaeva, Reaction cross sections for ^8B , ^7Be , and $^6\text{Li}+^{58}\text{Ni}$ near the Coulomb barrier: Proton-halo effects, *Phys. Rev. C* **79**, 021601(R) (2009).
- [41] R. Spartá, A. Di Pietro, P. Figuera, O. Tengbland, I. Martel *et al.*, Probing proton halo effects in the $^8\text{B}+^{64}\text{Zn}$ collision around the Coulomb barrier, *Phys. Lett. B* **820**, 136477 (2021).
- [42] M. Mazzocco, N. Keeley, A. Boiano, C. Boiano, M. La Commará *et al.*, Elastic scattering for the ^8B and $^7\text{Be}+^{208}\text{Pb}$ systems at near-Coulomb barrier energies, *Phys. Rev. C* **100**, 024602 (2019).
- [43] L. West, Jr., K. W. Kemper, and N. R. Fletcher, Elastic scattering of ^{16}O by even mass nickel isotopes, *Phys. Rev. C* **11**, 859 (1975).
- [44] M. A. G. Alvarez, L. C. Chamon, D. Pereira, E. S. Rossi, Jr., C. P. Silva, L. R. Gasques, H. Dias, and M. O. Roos, Experimental determination of the ion-ion potential in the $N = 50$ target region: A tool to probe ground-state nuclear densities, *Nucl. Phys. A* **656**, 187 (1999).
- [45] F. Videbæk, R. B. Goldstein, L. Grodzins, S. G. Steadman, T. A. Belote, and J. D. Garrett, Elastic scattering, transfer reactions, and fission induced by ^{16}O ions on ^{181}Ta and ^{208}Pb , *Phys. Rev. C* **15**, 954 (1977).
- [46] K. O. Pfeiffer, E. Speth, and K. Bethge, Break-up of ^6Li and ^7Li on tin and nickel nuclei, *Nucl. Phys. A* **206**, 545 (1973).
- [47] A. M. Sánchez-Benítez, D. Escrig, M. A. G. Álvarez, M. V. Andrés, C. Angulo *et al.*, Scattering of ^6He at energies around the Coulomb barrier, *J. Phys. G: Nucl. Part. Phys.* **31**, S1953 (2005).
- [48] A. M. Sánchez-Benítez (private communication).
- [49] J. J. Kolata, V. Z. Goldberg, L. O. Lamm, M. G. Marino, C. J. O’Keeffe, G. Rogachev, E. F. Aguilera, H. García-Martínez, E. Martínez-Quiroz, P. Rosales, F. D. Becchetti, T. W. O’Donnell, D. A. Roberts, J. A. Brown, P. A. DeYoung, J. D. Hinnefeld, and S. A. Shaheen, Elastic scattering and transfer in the $^8\text{Li}+^{208}\text{Pb}$ system near the Coulomb barrier, *Phys. Rev. C* **65**, 054616 (2002).
- [50] B. T. Kim, W. Y. So, S. W. Hong, and T. Udagawa, Simultaneous optical model analyses of elastic scattering, breakup, and fusion cross section data for the $^6\text{He}+^{209}\text{Bi}$ system at near-Coulomb-barrier energies, *Phys. Rev. C* **65**, 044607 (2002).
- [51] L. F. Canto, P. R. S. Gomes, J. Lubian, L. C. Chamon, and E. Crema, Disentangling static and dynamic effects of low breakup threshold in fusion reactions, *J. Phys. G* **36**, 015109 (2009).
- [52] J. M. N. Shorto, P. R. S. Gomes, J. Lubian, L. F. Canto, S. Mukherjee, and L. C. Chamon, Reaction functions for weakly bound systems, *Phys. Lett. B* **678**, 77 (2009).
- [53] P. R. S. Gomes, J. Lubian, I. Padron, and R. M. Anjos, Uncertainties in the comparison of fusion and reaction cross sections of different systems involving weakly bound nuclei, *Phys. Rev. C* **71**, 017601 (2005).
- [54] C. Y. Wong, Interaction barrier in charged-particle nuclear reactions, *Phys. Rev. Lett.* **31**, 766 (1973).
- [55] P. R. Christensen, V. I. Manko, F. D. Becchetti, and R. J. Nickless, A study of $^{16,18}\text{O}$ and ^{12}C induced reactions on $A = 40\text{--}96$ nuclei, *Nucl. Phys. A* **207**, 33 (1973).
- [56] E. F. Aguilera, J. J. Kolata, and L. Acosta, Evidence for core-halo decoupling in halo systems, *Phys. Rev. C* **81**, 011604(R) (2010).
- [57] O. Sgouros, V. Soukeras, K. Palli, and A. Pakou, Global approach for the reactions $^7\text{Be}+^{28}\text{Si}$ and $^7\text{Be}+^{208}\text{Pb}$ at near- and sub-barrier energies, *Phys. Rev. C* **106**, 044612 (2022).
- [58] A. Pakou, Global optical potential for ^7Be on various targets at sub- and near-barrier energies, *Phys. Rev. C* **109**, 014609 (2024).
- [59] A. Pakou, N. Alamanos, G. Doukelis, A. Gillibert, G. Kalyva *et al.*, Elastic scattering of $^7\text{Li}+^{28}\text{Si}$ at near-barrier energies, *Phys. Rev. C* **69**, 054602 (2004).
- [60] A. Pakou, N. Alamanos, A. Lagoyannis, A. Gillibert, E. C. Pollacco *et al.*, Elastic scattering of $^7\text{Li}+^{28}\text{Si}$ at near-barrier energies, *Phys. Lett. B* **556**, 21 (2003).
- [61] H. Esbensen and G. E. Bertsch, Effects of E2 transitions in the Coulomb dissociation of ^8B , *Nucl. Phys. A* **600**, 37 (1996).
- [62] A. J. Koning and J. P. Delaroche, Local and global nucleon optical models from 1 keV to 200 MeV, *Nucl. Phys. A* **713**, 231 (2003).
- [63] I. J. Thompson, Coupled reaction channels calculations in nuclear physics, *Comput. Phys. Rep.* **7**, 167 (1988).